Polarization-insensitive surface mode excitation on metamaterial-terminated one-dimensional photonic crystals

Polarization-insensitive surface mode excitation on metamaterial-terminated one-dimensional photonic crystals

Journal of Physics: Photonics

OPEN ACCESS

RECEIVED
24 March 2025

REVISED
30 April 2025

ACCEPTED FOR PUBLICATION
14 May 2025

PUBLISHED
23 May 2025

PAPER

Polarization-insensitive surface mode excitation on metamaterial-terminated one-dimensional photonic crystals

Tian-Long Guo[1,*], Behnaz Fazlpour[1], Markku Kuittinen[1], Emiliano Descrovi[2] and Matthieu Roussey[1]

[1] Center for Photonics Sciences, University of Eastern Finland, PO Box 111, FI-80101 Joensuu, Finland
[2] Department of Applied Science and Technology, Politecnico di Torino, 10129 Torino, Italy
[*] Author to whom any correspondence should be addressed.

E-mail: tianlong.guo@uef.fi

Keywords: photonic crystal, metamaterial, Bloch surface wave, effective medium approximation, polarization

Abstract

The use of a nanolaminate metamaterial exhibiting a subwavelength periodic pattern is demonstrated to tailor a one-dimensional photonic crystal (1DPC) in such a way that both transverse electric and magnetic surface modes can be simultaneously excited in the VIS-NIR range. In this framework, we provide a detailed analysis of the structure design by means of a combined use of the effective medium approximation and three-dimensional finite element method. Fabrication feasibility and limitations are considered, particularly in keeping into account the available materials. The tunability of the design and the capability of the 1DPC platform in controlling polarization states can suggest new approaches for polarization-resolved sensing on photonic chips.

1. Introduction

Bloch surface waves (BSWs) [1–4] are surface electromagnetic waves [5] possibly sustained by a truncated dielectric multilayer (ML), also called one-dimensional photonic crystal (1DPC) [6]. Such a ML typically consists of a periodic arrangement of subwavelength layers of high and low refractive index materials. Application-wise, BSWs offer numerous advantages over other types of surface waves, such as Rogue waves or surface plasmon polaritons. For example, BSW propagation length can extend to centimeters due to applying only the dielectric materials and deposition techniques [7]. And it enables the possibility of exploiting emission enhancement mechanisms without quenching [8, 9]. Moreover, the polarization states can be either transverse electric (TE) or transverse magnetic (TM) [10, 11]. These features make BSWs particularly useful for various applications, especially optical sensing [12–17]. However, for a fixed number of 1DPC layers, a significant difference in the BSW resonance amplitude is observed between the two polarizations, and TE and TM BSW dispersion do not overlap under ordinary conditions, which limits its implementation in, for example, signal enhancement for circular dichroism spectroscopy [11, 18, 19]. One solution is to introduce an additional anisotropic termination ML to the 1DPC, enabling an engineering of the dispersion relations of the TE and TM surface modes and superpose them coherently [10, 11].

In this work, we address the challenge of designing a flexible metamaterial-terminated 1DPC (MM-1DPC) platform capable of sustaining both TE and TM surface modes simultaneously. It is well established that subwavelength structures, such as nanolaminates (NLs) and subwavelength gratings (SWGs), are well-suited for creating birefringent components [20, 21]. By combining NL and SWG into a MM topping the 1DPC last interface, we can introduce the necessary birefringence and additional degrees of freedom in the design [22], which is crucial for tailoring the TE and TM mode dispersions independently.

While the effective medium approximation (EMA) models for NL and SWG are well-defined, they assume the constituent materials as isotropic. Given the complexity of the proposed structure, designs obtained from a mere application of the EMA model need to be refined using three-dimensional finite element methods (3D-FEMs) or finite-difference time-domain (3D-FDTD) models, so that a full overlapping of surface modes for both TE and TM polarizations is achieved.

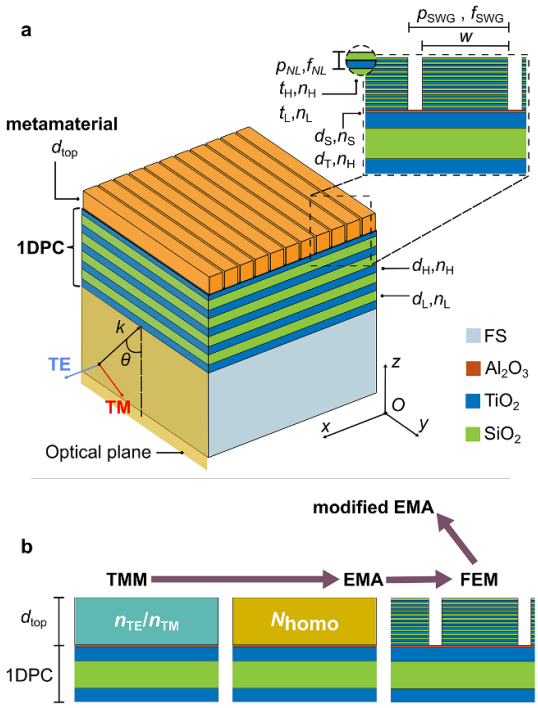

Figure 1. (a) A schematic representation of the metamaterial-terminated 1DPC platform, wherein the illumination is provided through TE and TM linearly polarized waves propagating from the bottom fused silica substrate. The orange-coloured part corresponds to the metamaterial illustrated in the inset. (b) Workflow diagram illustrating the multi-step design methodology employed. Initial target effective refractive indices (n_{TE}/n_{TM}) are found using TMM, assuming a homogeneous isotropic top layer (left). These guide the determination of target anisotropic refractive indices (N_{homo}) for a homogeneous anisotropic layer (middle). Standard EMA provides initial estimates for filling factors (f_{SWG},f_{NL}), which are then refined through iterative 3D-FEM optimization of the actual structured MM layer (right) to achieve simultaneous TE/TM excitation. The relationship found via FEM informs the derivation of the modified EMA. The schematics below the workflow illustrate the different top layer models considered: isotropic homogeneous, anisotropic homogeneous, and the final metamaterial, on the 1DPC base.

In the following, we propose an efficient and feasible design method enabling a comprehensive design of a MM-terminated 1DPC platform, wherein both TE and TM surface modes can be coupled simultaneously.

2. Principle and design

We consider the MM-1DPC illustrated in figure 1. It consists of a stack of alternating high refractive index (n_H) and low refractive index (n_L) materials over four film pairs and a truncation layer of refractive index n_H with thickness d_T. On top of the truncation layer, a MM layer with thickness d_{top} is included. The MM comprises a NL having a stack period p_{NL}, patterned with grooves extended in the y-direction and periodically arranged along the x-direction with a grating period p_{SWG}. The MM-1DPC is assumed to be deposited on a fused silica substrate. All raw materials considered here are selected from our in-house manufacturing capabilities. Refractive indices used in the calculations are taken from ellipsometry measurements on single layers deposited on purpose. Specifically, TiO_2 is chosen as the high refractive index and SiO_2 as the low refractive index. To provide a realistic design suitable for fabrication, a thin ($d_S = 10$ nm) Al_2O_3 spacer layer is also included between the truncation layer and the MM layer, acting as an etch-stop layer during the patterning process. The entire MM-1DPC structure, starting from the glass substrate is: $(TiO_2 + SiO_2) \times 4 + TiO_2 + Al_2O_3 + MM$ with thickness of $(d_H + d_L) \times 4 + d_T + d_S + d_{top}$.

In the following, we refer to filling factors $f_{NL} = t_H/p_{NL}$ and $f_{SWG} = w/p_{SWG}$, where t_H and w are the thickness of the high refractive index material in the NL structure and the width of the ridge in the SWG, respectively. Since the main focus here is on the design of the MM layer, our target is represented by an exemplary underlying 1DPC providing BSWs at a fixed wavelength $\lambda_0 = 532$ nm and excitation angle $\theta = 76°$ for both TE and TM illuminations. As it will be apparent in the following, our approach can be easily adapted to other desired conditions as well. As depicted in figure 1, the TE polarization means that the electric field **E** is oriented in x- direction only (i.e. perpendicular to the SWG), while TM polarization refers to magnetic field **H** oriented in x- direction only. Herein, the following refractive indices are used: $n_H = n_{TiO_2} = 2.4256 + ik$, $n_L = n_{SiO_2} = 1.4579 + ik$, $n_S = n_{Al2O3} = 1.6331 + ik$, $n_{sub} = 1.46$, where $k = 10^{-4}$ to account for all losses, including absorption, scattering, and leakage [23]. The geometry parameters for the

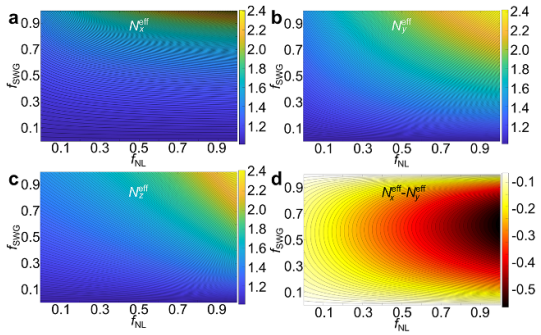

Figure 2. Calculated using EMA model: Effective refractive indices maps of the MM in the (a) x-, (b) y-, and (c) z- axis with f_{NL} and f_{SWG} varying from 0.01 to 0.99. (d) is the $N_x^{eff} - N_y^{eff}$ map in the same filling factor range. The contour step is 0.01 for all maps.

1DPC are set to be four pairs of two alternating layers of $d_H = 114$ nm of TiO_2 and $d_L = 140$ nm of SiO_2 covered by the truncated TiO_2 film. Introducing a truncated layer is beneficial for design, as it adjusts the MM layer specifications (thickness, refractive index) that are needed to couple the surface mode with a specific 1DPC. And its thickness is set as $d_T = 72$ nm.

Since there is no rotation/tilting of the MM layer, both the NL and SWG have the periodic structure direction aligned with the Cartesian coordinates; thus, the optical axes of the MM align well in the x-, y- and z- axes shown in figure 1. Given the MM geometry and constituent materials, the effective indices of the NL layer alone can be defined according to the EMA model [20] as follows:

$$N_x^{NL} = N_y^{NL} = \left(f_{NL} n_{TiO_2}^2 + (1 - f_{NL}) n_{SiO_2}^2\right)^{\frac{1}{2}} \tag{1a}$$

$$N_z^{NL} = \left(f_{NL} n_{TiO_2}^{-2} + (1 - f_{NL}) n_{SiO_2}^{-2}\right)^{-\frac{1}{2}}. \tag{1b}$$

However, after the x-oriented SWG is inscribed into the NL layer, further optical anisotropy in the xy-plane is obtained. The effective refractive indices along the x-, y-, and z- directions can be described according to equations (2a), (2b) and (2c)[21]:

$$N_x^{eff} = \left(f_{SWG} \left(N_x^{NL}\right)^{-2} + (1 - f_{SWG})\right)^{-\frac{1}{2}} \tag{2a}$$

$$N_y^{eff} = \left(f_{SWG} \left(N_y^{NL}\right)^{2} + (1 - f_{SWG})\right)^{\frac{1}{2}} \tag{2b}$$

$$N_z^{eff} = \left(f_{SWG} \left(N_z^{NL}\right)^{2} + (1 - f_{SWG})\right)^{\frac{1}{2}}. \tag{2c}$$

Note that since the imaginary part of the refractive index is negligible, we ignore it during the EMA modeling.

Figures 2(a)–(c) present the effective refractive indices of the MM along the x-, y-, and z- axis with filling factors f_{NL} and f_{SWG} varying from 0.01 to 0.99. Taking into account all possible combinations, effective indices N_x^{eff}, N_y^{eff}, and N_z^{eff} range from 1.2 to 2.4. Interestingly, N_y^{eff} is always larger than N_x^{eff}, as displayed in figure 2(d), where $N_y^{eff} - N_x^{eff}$ is shown to be always larger than 0.1, with values up to 0.5. Such refractive index relations in the three main axes of the artificial anisotropy MM are important guides for the anisotropic termination design.

Our specific design methodology, visually summarized in figure 1(b), employs a structured multi-step approach. First, we apply the transfer matrix method (TMM) assuming idealized homogeneous top layers (isotropic, then anisotropic) to determine the target effective refractive indices ($N_{homo} = \{N_x^{eff}, N_y^{eff}, N_z^{eff}\}$) required for simultaneous BSW excitation under the desired conditions. Second, we apply standard EMA formulas (equations (1a)–(2c)) to obtain initial estimates for the MM filling factors (f_{NL},f_{SWG}) that should theoretically produce N_{homo}. Third, recognizing the intrinsic limitations of TMM in accurately modeling the complex nanostructured MM layer, we perform rigorous 3D-FEM simulations. These FEM optimizations are methodologically essential for refining the design by systematically varying f_{NL} and f_{SWG}, for given p_{NL} and p_{SWG} to find the actual parameters yielding simultaneous TE/TM excitation. Finally, based on the divergence between the EMA predictions and the FEM optimizations, we will present a modified EMA formula that describes the detailed relationship between the effective refractive indices and the geometrical parameters. The details of our approach are described below.

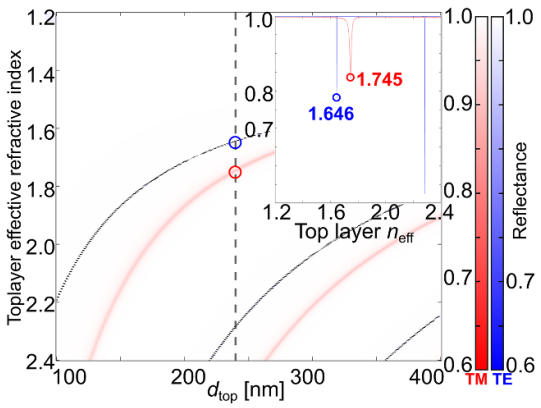

Figure 3. Superimposed reflectance map for TE (blue, overlapped with black dots for better visibility) and TM (red) illuminations. The incident angle is kept fixed at 76°, wavelength is $\lambda_0 = 532$ nm, and the top layer effective index is varied, as well as its thickness. Inset: Cross-sectional view of the reflectivity profiles of BSW dips with different n_{eff} for $d_{\text{top}} = 240$ nm, as shown by the dashed line in the map.

Homogeneous isotropic top layer

We start by treating the MM top layer as an isotropic, uniform film, with an effective refractive index of n_{TE} or n_{TM}, to couple with the specified 1DPC configuration defined in the previous section for the TE- or TM-BSW, respectively. The BSW dispersion (visible as a dip in the reflectance spectrum) in such a 1DPC depends on a combination of the top layer's effective refractive index n_{eff} (n_{TE} or n_{TM}) and thickness d_{top}. BSWs for both polarizations that correspond to different n_{eff} and d_{top} are found using the TMM and plotted in figure 3 [24]. As a design constraint, we impose $d_{\text{top}} = 240$ nm, based on a reasonable assumption of fabrication feasibility. In this configuration, the top layer shows distinct values of the effective refractive index to couple either TE- or TM-BSWs, specifically, $n_{\text{TE}} = 1.646 + ik$ for TE (blue) surface modes and $n_{\text{TM}} = 1.745 + ik$ for TM (red) surface mode, as apparent from the inset of figure 3.

Homogeneous anisotropic top layer

In order to sustain both TE and TM modes simultaneously under the same excitation conditions ($\lambda_0 = 532$ nm and $\theta = 76°$), the top layer of the 1DPC must exhibit birefringence. It is important to note that while anisotropy originates from specific geometric configurations, such as NL and SWG, the actual structure geometry is not explicitly considered in this step. Instead, a homogeneous yet birefringent top layer is assumed to determine the target anisotropic refractive indices.

First, we consider a simple configuration, where the optical anisotropy is applied on the *xOy*- plane only ($N_y^{\text{eff}} = N_z^{\text{eff}}$). This scenario corresponds to using a simple SWG made of an isotropic material, for instance, a 240 nm-thick top layer consisting of TiO_2 SWGs oriented along the *x*-axis. Such a structure produces uniaxial birefringence predictable by standard EMA. In figure 4(a), the effective refractive indices $N_x^{\text{eff}} = (f_{\text{SWG}}(n_{\text{TiO}_2})^{-2} + (1 - f_{\text{SWG}}))^{-\frac{1}{2}}$ and $N_y^{\text{eff}} = N_z^{\text{eff}} = (f_{\text{SWG}}(n_{\text{TiO}_2})^2 + (1 - f_{\text{SWG}}))^{\frac{1}{2}}$ are shown for f_{SWG} varying from 0.01 to 0.99. According to the EMA model, the TE mode is sensitive to N_x^{eff} while the TM mode is sensitive to $N_y^{\text{eff}} = N_z^{\text{eff}}$. Since TiO_2 is a high refractive index material, N_x^{eff}, N_y^{eff}, and N_z^{eff} span a range that includes the target values for n_{TE} and n_{TM} previously found. However, as clearly illustrated in figure 4(a), there is no single filling factor f_{SWG} for which the structure simultaneously satisfies the required effective refractive index conditions for both TE ($N_x^{\text{eff}} = n_{\text{TE}} = 1.646$, blue dashed line) and TM ($N_y^{\text{eff}} = N_z^{\text{eff}} = n_{\text{TM}} = 1.745$, red dashed line) modes. This demonstrates that the uniaxial anisotropy provided by a simple SWG offers insufficient degrees of freedom for our purpose. To overcome this limitation and gain the necessary design flexibility, the NL structure is combined with the SWG. As will be shown, this NL/SWG combination allows engineering on a biaxial effective medium, providing the additional control required to satisfy both TE and TM conditions independently.

Therefore, we now consider a homogeneous biaxial birefringence medium with anisotropy on *x*-, *y*-, and *z*-axes, i.e. having diagonal refractive indices: $N_{\text{homo}} = \{N_x^{\text{eff}}, N_y^{\text{eff}}, N_z^{\text{eff}}\}$. Ideally, we initially targeted the indices $N_x^{\text{eff}} = n_{\text{TE}} = 1.646$ and $N_y^{\text{eff}} = N_z^{\text{eff}} = n_{\text{TM}} = 1.745$ based on the isotropic case (figure 3) for $d_{\text{top}} = 240$ nm. Unfortunately, applying the standard EMA model reveals that no combination of $(f_{\text{NL}}, f_{\text{SWG}})$ can simultaneously yield exactly these target indices. Note that the components of the effective refractive index N_{homo} are linked through equations (1*a*)–(2*c*) and the steps to find $(f_{\text{NL}}, f_{\text{SWG}})$ for the anisotropic layer starts with matching N_x^{eff} for TE surface mode. The condition for coupling TE-polarized BSW is enforced by assuming $N_x^{\text{eff}}(f_{\text{NL}}, f_{\text{SWG}}) = n_{\text{TE}} = 1.646$, since the $\mathbf{E}_{\text{TE}}$ only has one component in *x*- axis. Instead, for

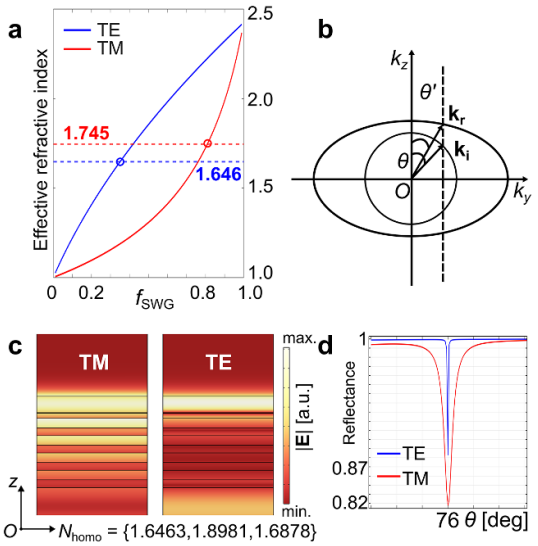

Figure 4. (a) Calculated using standard EMA for a TiO_2 SWG-only top layer: Effective refractive index as a function of f_{SWG} for TE mode (N_x^{eff}, blue line) and TM mode ($N_y^{eff} = N_z^{eff}$, red line). The horizontal dashed lines indicate the target effective indices $n_{TE} = 1.646$ and $n_{TM} = 1.745$ identified from figure 3. (b) The k surface of the substrate (circle) and the anisotropic top layer (ellipse). The $\mathbf{k}_i$ represents the incident wavevector from the substrate, and the $\mathbf{k}_r$ shows the refracted wavevector in the anisotropic layer following Snell's law. (c) Distribution of the electric field norm, $|\mathbf{E}|$ in the zOy plane cross-section for the BSW mode, with the top layer modeled as an anisotropic material with refractive indices $\{N_x^{eff}, N_y^{eff}, N_z^{eff}\} = \{1.6463, 1.8981, 1.6878\}$. (d) Reflectance spectra of the TE and TM modes presented in (c), showing simultaneous excitation at $\theta = 76°$.

TM-polarized BSW, both N_y^{eff} and N_z^{eff} must be taken into account because the TM-polarized BSW has components in both y- and z- directions. The effective refractive index for TM-polarization is given by:

$$\frac{1}{n_{eff}^2(\theta')} = \frac{\cos^2\theta'}{N_y^{eff2}} + \frac{\sin^2\theta'}{N_z^{eff2}}, \tag{3}$$

where θ' is the propagation angle within the top layer. As a further constraint, the Snell's law (equation (4)) must be imposed in order to keep the phase matching between the incident radiation and the BSW, as schematically shown in figure 4(b):

$$n_{sub}\sin\theta = n_{eff}(\theta')\sin\theta', \tag{4}$$

where θ is the incident angle from the substrate.

After applying the constraints above and performing calculations using a TMM model incorporating the anisotropic layer, the condition for the simultaneous coupling of BSW from 1DPC in both polarizations is achieved with the 240 nm-thick top layer having refractive index $N_{homo} = \{1.6463, 1.8981, 1.6878\}$, when illuminated by a 532 nm plane wave at an angle of 76°. This slightly adjusted set of indices becomes our target for the MM design. In figure 4(c), the $|\mathbf{E}|$ the cross-sectional distribution in the zOy plane shows an energy localization close to the surface both in TE- and TM-polarizations, as expected from BSW. In reflectivity, the simultaneous coupling is demonstrated by the overlapping of the two resonant dips, as shown in figure 4(d).

Metamaterial top layer

To implement the required anisotropic properties, the 3D geometry of the MM terminated 1DPC is analyzed using the FEM software COMSOL Multiphysics. This allows rigorous validation and refinement beyond the idealized EMA and homogeneous layer models. The 'Electromagnetic Waves, Frequency Domain' physics was used to compute the electric field distribution through a full-field formulation.

A 3D model of a unit cell of the MM, together with the 1DPC and the substrate underneath correlating with the coordinate system shown in figure 1, was constructed. To minimize the model's size, the length of the grating along the y-axis was set to 20 nm, while the width of the unit cell along the x-axis was set as p_{SWG}. The dielectric materials were stacked in a sequence as outlined in the earlier section. Incident radiation is introduced from a port located at the bottom of the geometry (substrate side). Transmission is assessed using a monitor placed at the top of the structure, while reflection is measured through the input port. To ensure an accurate evaluation, the wave propagation distance outside the MM-1DPC—specifically, the distance from the top monitor to the MM surface and from the bottom port to the bottom layer of the 1DPC—is maintained at least half a wavelength apart. To achieve the MM periodicity using a unit cell, Floquet periodic

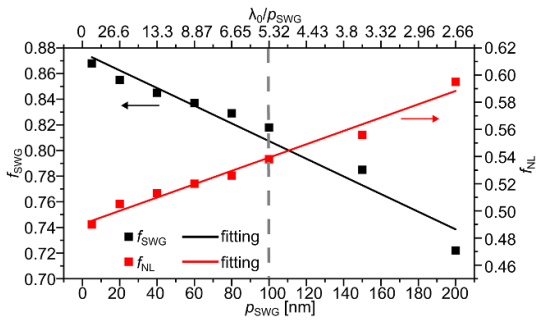

Figure 5. Results from 3D-FEM optimization: f_{SWG} and f_{NL} values (points) with their linear fitting lines for the metamaterial top layer as a function of SWG period p_{SWG} responsible for achieving simultaneous excitation of TE- and TM-BSW modes on the 1DPC at $\theta = 76°$ and $\lambda_0 = 532$ nm.

Table 1. Filling factors for different periodicities of SWG.

Sample code	p_{SWG} [nm]	f_{NL}	f_{SWG}
P5	5	0.49	0.868
P20	20	0.505	0.855
P40	40	0.513	0.845
P60	60	0.520	0.837
P80	80	0.526	0.829
P100	100	0.538	0.818

boundaries were assigned to the lateral faces of the physical domain in the *xOy* plane. We selected a suitable mesh quality to balance result accuracy and computational efficiency after a mesh convergence study discussed in the appendix and illustrated in figure 8.

3. Results and discussion

One of the assumptions in the EMA description is that the nanostructure size, specifically the parameters p_{NL} and p_{SWG}, should be sub-wavelength ($p_{NL} \ll \lambda_0$ and $p_{SWG} \ll \lambda_0$). To simplify the study, we will keep the NL periodicity, p_{NL} constant at 20 nm while varying the SWG periodicity, p_{SWG}, from 5 nm to 200 nm. This variation allows us to explore the applicability of EMA in MM design. It is important to notice that the upper limit of 200 nm exceeds the valid range for EMA ($\lambda_0/p_{SWG} = 2.66$). However, our goal is not only to achieve theoretical validation but also to realize designs that are feasible for fabrication. Therefore, investigating designs with larger periodicities remains worthwhile.

Since our goal is to achieve specific refractive index values, $N_{homo} = \{1.6463, 1.8981, 1.6878\}$, we first calculated the filling factors f_{SWG} and f_{NL} of the MM top layer using equations (1*a*)–(2*c*). As a result, solving these equations for the target N_{homo} yields $f_{SWG} = 0.833$ and $f_{NL} = 0.532$. According to the standard EMA model, the MM top layer with these filling factors should couple with the 1DPC mentioned above, supporting both TE and TM BSW modes under identical excitation conditions, regardless of the values of p_{NL} and p_{SWG}, as long as they fall within the range specified by the EMA constrain. However, when we evaluated the actual 3D model in COMSOL, our initial assumption proved to be invalid. Specifically, for each value of p_{SWG}, we needed to optimize and determine a new pair of f_{SWG} and f_{NL} values via FEM simulations to achieve simultaneous excitation. The calculated f_{SWG} and f_{NL} pairs for specific p_{SWG} values from 5 nm to 200 nm are plotted in figure 5 to illustrate such variation. Moreover, a linear fitting for both f_{SWG} and f_{NL} values was also performed and illustrated as solid lines in the figure.

Contrary to expectations, both the f_{SWG} and f_{NL} exhibit a linear variation trend, rather than remaining constant, even when the p_{SWG} is less than 100 nm, where $\lambda_0/p_{SWG} > 5.32$. Detailed values for p_{SWG} less than 100 nm are provided in table 1. Furthermore, when the p_{SWG} exceeds 100 nm, the filling factors are found to deviate more significantly from the linear fitting lines. This suggests that, while a linear approximation holds reasonably well for $p_{SWG} \leqslant 100$ nm, it remains challenging to accurately predict the actual filling factors when p_{SWG} is too large using simple models. Taking this into consideration, the following study will focus on establishing the relationship between SWG periodicity and filling factors, as well as the effective refractive index of the MM, only within the range where p_{SWG} is between 5 and 100 nm.

The observed linear trends in both f_{NL} and f_{SWG} as the periodicity of the SWG increases suggest that the standard EMA formulas, represented by equations (1*a*)–(2*c*), cannot be used to directly predict the optimal

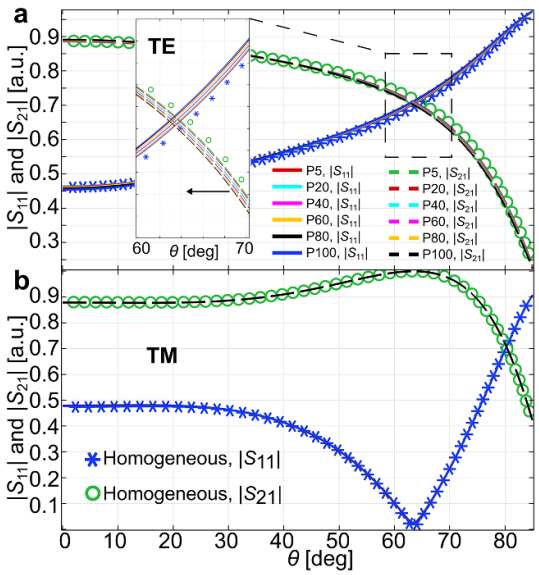

Figure 6. FEM simulated comparison of optical response versus angle of incidence (θ) at $\lambda_0 = 532$ nm: The magnitude of reflection ($|S_{11}|$) (solid lines for MM, stars for homogeneous) and transmission ($|S_{21}|$) (dashed lines for MM, circles for homogeneous) for different structured metamaterial layers (240 nm-thick, p_{SWG} from 5 to 100 nm, with corresponding filling factors listed in table 1) are compared to the homogeneous anisotropic layer (240 nm-thick) with target effective indices $N_{\mathrm{homo}} = \{1.6463, 1.8981, 1.6878\}$. The incident wavelength λ_0 is 532 nm, and the incident angle varies from 0° to 85°. (a) TE polarization, and (b) TM polarization. The enlarged view of (a), from 60° to 70°, is shown in the inset. Both (a) and (b) share the same sample legends. Note that in (b), all the solid lines and dashed lines perfectly overlap with stars and circles, respectively. This figure assesses how well the structured MM layers mimic the optical response of the effective anisotropic homogeneous medium.

filling factors found via FEM. Furthermore, when the size of the nanostructure changes (p_{SWG}), the filling factors must also be adjusted accordingly to maintain the simultaneous excitation condition. It is important to understand that the sensitivity of the all-dielectric platform that supports surface mode is relatively high. For instance, a detection limit of 7.5×10^{-7} refractive index units has been reported for a similar SiO_2/TiO_2 stack [25]. Consequently, even a slight variation in the refractive index of the top layer can result in a significant angular shift for the surface mode(s), which must be compensated for by adjusting the filling factors.

To understand the details of this mechanism and formulate new formulas that represent the relation between the p_{SWG} and the filling factors accurately, we further investigate the optical properties of the MM layer alone (240 nm-thick, listed in table 1) and compare them with those of the anisotropic homogeneous top layer (240 nm-thick, with $N_{\mathrm{homo}} = \{1.6463, 1.8981, 1.6878\}$) in FEM models. Specifically, we evaluate the $|S_{11}|$ (reflection) and $|S_{21}|$ (transmission) values for such layers (sandwiched by air) at a wavelength of 532 nm, using a linearly polarized incident wave, while varying the angle of incidence from 0° to 85°, as shown in figure 6. Figure 6(a) and b present the same model geometry, differing only in the polarization of the incident waves, consequently, both panels share the same legends.

In figure 6(a), which illustrates the samples under TE polarization, we observe a slight shift in the $|S_{11}|$ (solid) and $|S_{21}|$ (dashed) curves as the SWG period p_{SWG} varies. Since only N_x^{eff} is probed by the TE mode, this shift of $|S_{11}|$ and $|S_{21}|$ with different incident angles suggests that the N_x^{eff} values of the structured layers are dependent on p_{SWG} and differ slightly from the target value $N_x^{\mathrm{eff}} = 1.6463$ in N_{homo}.

In contrast, figure 6(b) shows the samples under TM polarization, where the lines representing both $|S_{11}|$ (solid) and $|S_{21}|$ (dashed) values across different MM configurations overlap perfectly with stars and circles (homogeneous sample), respectively. This indicates that the effective optical response related to the combination of N_y^{eff} and N_z^{eff} remains consistent with the target N_y^{eff} and N_z^{eff} in N_{homo}, and is largely independent of p_{SWG} in this range.

The study above provides valuable insights for modifying the standard EMA formulas to better estimate the filling factors with a varying p_{SWG}. To achieve this, based on the observed p_{SWG}-dependence for TE (figure 6(a)) and independence for TM (figure 6(b)), we introduce a first-order polynomial correction function to N_x^{eff}: $A(p_{\mathrm{SWG}}) = a_1 \cdot p_{\mathrm{SWG}} + a_2$, where a_1 is a dimensional coefficient with a unit of nm^{-1}, a_2 is a dimensionless constant, and the unit of the SWG periodicity p_{SWG} is in nanometers. Meanwhile, we use constant off-set corrections B and C for N_y^{eff} and N_z^{eff}, respectively, to represent their observed independence of p_{SWG}.

By fitting these correction terms (a_1, a_2, B, C) to the FEM optimization results presented in table 1, i.e. finding the corrections needed such that the EMA model will describe well the effective refractive indices by the f_{NL}, f_{SWG} pairs for each p_{SWG}, we formulated the modified EMAs for the proposed MM on 1DPC in figure 1, valid for $p_{SWG} \in [5, 100]$ nm for this specific 1DPC and material system:

$$N_x^{eff} = \left(f_{SWG}\left(N_x^{NL}\right)^{-2} + (1 - f_{SWG})\right)^{-\frac{1}{2}} + 0.00072 p_{SWG} + 0.04308 \qquad p_{SWG} \in [5, 100] \tag{5a}$$

$$N_y^{eff} = \left(f_{SWG}\left(N_y^{NL}\right)^{2} + (1 - f_{SWG})\right)^{\frac{1}{2}} + 0.0062 \tag{5b}$$

$$N_z^{eff} = \left(f_{SWG}\left(N_z^{NL}\right)^{2} + (1 - f_{SWG})\right)^{\frac{1}{2}} + 0.00718. \tag{5c}$$

It is crucial to understand that these modified EMA equations are empirical descriptions derived from fitting the FEM results. They accurately represent the required relationship between the filling factors and the SWG period within the studied range for this specific structure, but they do not serve as a predictive tool for arbitrary structures or conditions without prior FEM validation. The modified EMAs are checked with different anisotropic top layer cases (see table 2 in the appendix). It is noted that the modified EMA performs well with samples S1 and S2, in which the top layer thickness and the excitation condition (incident angle) are changed, respectively. However, for sample S3, the materials' refractive indices are different from the samples above due to dispersion, and the 1DPC truncation layer is different, so a new set of modified EMA correction factors is needed. Following the same fitting procedure based on FEM results for S3, the modified EMA expressions are:

$$N_x^{eff} = \left(f_{SWG}\left(N_x^{NL}\right)^{-2} + (1 - f_{SWG})\right)^{-\frac{1}{2}} + 0.00116 p_{SWG} + 0.01023 \qquad p_{SWG} \in [5, 100]$$

$$N_y^{eff} = \left(f_{SWG}\left(N_y^{NL}\right)^{2} + (1 - f_{SWG})\right)^{\frac{1}{2}} + 0.05938$$

$$N_z^{eff} = \left(f_{SWG}\left(N_z^{NL}\right)^{2} + (1 - f_{SWG})\right)^{\frac{1}{2}} + 0.05175.$$

The findings regarding the different modified EMA formulas for sample S3 indicate that the correction terms are structure- and condition-specific, confirming that the traditional EMA is not readily suited for precise design of MMs that exhibit biaxial properties. Additionally, there is no general solution or universally applicable correction factor available for such specific modifications without performing targeted FEM simulations. Finally, it should be noted that in this study, we focus on formulating the modified EMA formulas with p_{SWG} ranging from 5 to 100 nm.

Regarding fabrication feasibility, in figure 5, f_{SWG} decreases linearly from approximately 0.86 to 0.72, while f_{NL} increases linearly from around 0.48 to 0.60, as p_{SWG} increases. Precise control of f_{NL} can be achieved by techniques such as atomic layer deposition [26]. However, using lithography methods like e-beam lithography and reactive ion etching for SWG, achieving features less than 10 nm is challenging. Thus, for a practical fabrication scheme, patterning the gratings on the NL with a p_{SWG} exceeding 100 nm is more feasible. As a trade-off, we choose $p_{SWG} = 100$ nm to study its full optical properties.

Figure 7(a) shows the superimposed reflectance spectra map of the MM-1DPC under TE- (blue) and TM-polarized (red) incidents from 3D-FEM simulation. The MM has a grating periodicity of $p_{SWG} = 100$ nm and $p_{NL} = 20$ nm, and optimized filling factors of $f_{NL} = 0.538$ and $f_{SWG} = 0.818$. The incident angle is varied from 40° to 87°. We considered the full dispersion of the materials measured from the ellipsometer and calculated the reflectance spectra of the MM-1DPC from 500 nm to 600 nm. Both TE and TM modes overlap well across the spectrum. The overlapping point at $\theta = 76°$ and $\lambda_0 = 532$ nm is denoted using a black dot on the map. Detailed TE/TM reflectance spectra at $\lambda_0 = 532$ nm for different incident angles are shown in figure 7(b1). Additionally, the electric field distribution inside the unit cell is presented in figure 7(c), exhibiting a more insightful view of both modes. The electric field intensity calculated from the center of the MM-1DPC also exhibits a surface mode-like behavior, showing an exponential decay of intensity from the surface.

Notably, when comparing the reflectance amplitude in figure 7(b1) to the inset in figure 3, the amplitude of the reflectance dips decreases. An additional study of recording reflectance values by rotating the incident wave azimuthally at $\theta = 76°$ and $\lambda_0 = 532$, shown in figure 7(b2), reveals that rotating the incident wave by 1.7° for TE illumination and 1.8° for TM illumination will significantly enhance the dip amplitude while the rotation direction does not affect the mode's position. We can surmise that the NL and SWG may affect the dip amplitude by creating multiple internal reflections inside the nanostructures, that a slight azimuthal rotation optimizes coupling under these conditions (inset figure 7(b2)).

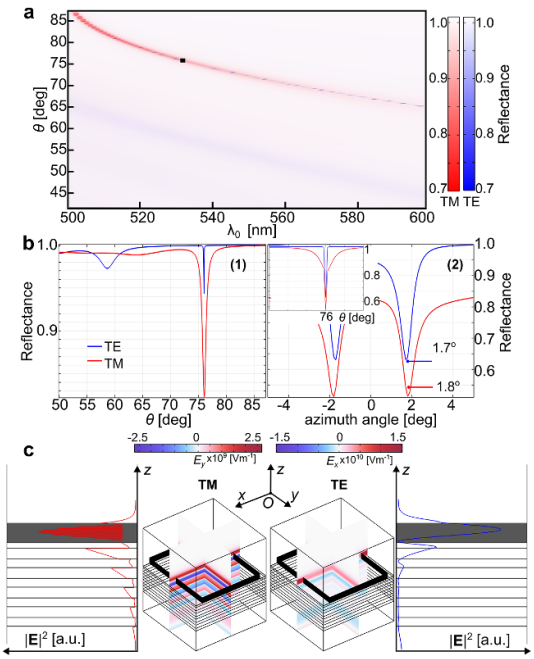

Figure 7. Simulated using 3D-FEM: The optical response of the MM-1DPC structure with a grating periodicity of $p_{SWG} = 100$ nm and $p_{NL} = 20$ nm, and filling factors being $f_{NL} = 0.538$ and $f_{SWG} = 0.818$. The total thickness of MM is 240 nm (a) superimposed reflectance map of the MM-1DPC under TE (blue) and TM (red) polarization, considering material dispersion. The black dot indicates $\theta = 76°$ and $\lambda_0 = 532$ nm condition. (b1) Reflectance spectra of the MM-1DPC under TE and TM polarization at different θ for $\lambda_0 = 532$ nm. (b2) Reflectance spectra of the MM-1DPC under TE and TM polarization at various azimuth angles with $\theta = 76°$ and $\lambda_0 = 532$ nm. Inset is the reflectance spectra for different θ at $\lambda_0 = 532$ nm when the azimuth angle is 1.7°. (c) Distribution of E_y and E_x inside an MM-1DPC 3D unit cell at TM- and TE-BSW modes, respectively. The $|E|^2$ measured through the center of a unit cell along the z-axis is also included for each mode, demonstrating field confinement near the surface.

4. Conclusion

In conclusion, we have demonstrated the design of a MM-terminated 1DPC, combining NL and SWG structures, capable of exciting polarization-insensitive BSWs. Our design strategy integrated initial estimates from TMM and standard EMA with essential refinement via rigorous FEM simulations. This process revealed the inadequacy of standard EMA for accurately modeling the complex NL+SWG structure, thus requiring the use of FEM for precise design predictions. Based on the FEM results, we developed modified empirical EMA formulas that better describe the system's behavior within the validated parameter range. This combined TMM/EMA-FEM approach proves effective for tackling similar complex photonic designs where simplified models may prove inadequate. The key limitations, however, include the computational demand of FEM and the empirical, structure-specific nature of the modified EMA corrections requiring re-derivation for different configurations. Methodologically, this work highlights a systematic process—using standard models, identifying their limitations via rigorous simulation, and developing corrections—that offers a broadly applicable strategy for designing and understanding complex photonic systems beyond the reach of first-order approximations and contributes to defining EMA's applicability boundaries.

Data availability statement

The data cannot be made publicly available upon publication because they are not available in a format that is sufficiently accessible or reusable by other researchers. The data that support the findings of this study are available upon reasonable request from the authors.

Acknowledgments

The authors wish to acknowledge CSC—IT Center for Science, Finland, for computational resources.

Conflicts of interest

The authors declare no conflicts of interest.

Funding

Research Council of Finland Flagship programme PREIN, decision 346 518. Project RAVEN funded by European Union's Horizon Europe research and innovation programme under grant agreement number 10 113 5787.

Appendix

A.1. Different cases for EMA validation

The entire MM-1DPC structure, starting from the glass substrate is: $(TiO_2 + SiO_2) \times 4 + TiO_2 + Al_2O_3 +$ MM with thickness of $(d_H + d_L) \times 4 + d_T + d_S + d_{top}$. This configuration is valid for all samples presented in table 2.

Table 2. Geometry configuration and excitation conditions for different samples.

Sample code	λ_0 [nm]	θ [deg]	d_T [nm]	d_{top} [nm]	N_{homo}
S0[a]	532	76	72	240	$\{1.6463, 1.8981, 1.6878\}$
S1	532	76	72	**220**	$\{1.6778, 1.9456, 1.7335\}$
S2	532	**75**	72	240	$\{1.639, 1.8815, 1.6726\}$
S3[b]	**632**	76	**20**	240	$\{1.4445, 1.7567, 1.5883\}$

[a] The proposed design in the main text.

[b] The dispersion is considered for the materials used for calculation.

A.2. Mesh convergence study

The reflectance at the TE surface mode condition is used as the monitor to observe the mesh convergence. Typically, the maximum mesh size is gradually decreased for better meshing quality, and the degree of freedom correlates directly with it by increasing. Figure 8 is the mesh convergence study when $p_{NL} = 20$ nm and p_{SWG} is 100 nm. It is clear that when the maximum mesh size is 20 nm (red square) or even less, the reflectance varies within $\pm 1\%$ (gray area in the figure). To save the calculation resources and study time, the maximum mesh size of 20 nm is used.

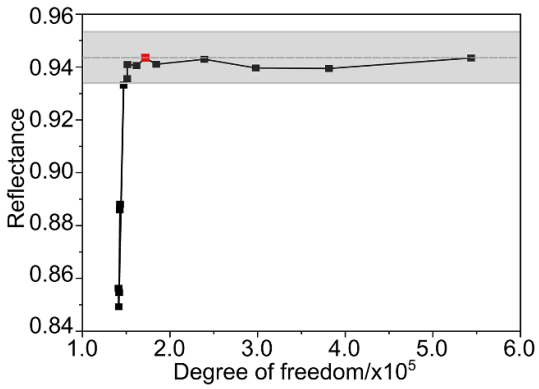

Figure 8. Mesh convergence study. Reflectance value of the MM-1DPC at 76° incidence of TE polarized light at 532 nm. The degree of freedom is directly related to the maximum mesh size of the model. The red point and the dashed line denote the mesh quality selected for calculating $p_{SWG} = 100$ nm model where the maximum mesh size is 20 nm and the reflectance value, respectively. The gray area represents values $\pm 1\%$ deviate from the red point.

ORCID iDs

Tian-Long Guo https://orcid.org/0009-0000-2969-4315
Markku Kuittinen https://orcid.org/0000-0002-5334-6844
Emiliano Descrovi https://orcid.org/0000-0002-3613-2967
Matthieu Roussey https://orcid.org/0000-0002-7679-6995

References

[1] Robertson W M 1999 Experimental measurement of the effect of termination on surface electromagnetic waves in one-dimensional photonic bandgap arrays *J. Lightwave Technol.* **17** 2013–7
[2] Robertson W M and May M S 1999 Surface electromagnetic wave excitation on one-dimensional photonic band-gap arrays *Appl. Phys. Lett.* **74** 1800–2
[3] Villa F and Gaspar-Armenta J A 2004 Photonic crystal to photonic crystal surface modes: narrow-bandpass filters *Opt. Express* **12** 2338–55
[4] Liscidini M and Sipe J E 2007 Enhancement of diffraction for biosensing applications via Bloch surface waves *Appl. Phys. Lett.* **91** 253125
[5] Polo J A and Lakhtakia A 2011 Surface electromagnetic waves: a review *Laser Photon. Rev.* **5** 234–46
[6] Yeh P, Yariv A and Cho A Y 1978 Optical surface waves in periodic layered media *Appl. Phys. Lett.* **32** 104–5
[7] Vosoughi Lahijani B, Descharmes N, Barbey R, Osowiecki G D, Wittwer V J, Razskazovskaya O, Südmeyer T and Peter Herzig H 2022 Centimeter-scale propagation of optical surface waves at visible wavelengths *Adv. Opt. Mater.* **10** 2102854
[8] Tang Z, Guo T-L, Augenstein Y, Troia A, Liu Y, Roussey M, Rockstuhl C and Descrovi E 2024 Coupling light into a guided Bloch surface wave using an inversely designed nanophotonic cavity *Appl. Phys. Lett.* **125** 181103
[9] Michelotti F and Sepe E 2019 Anisotropic fluorescence emission and photobleaching at the surface of one-dimensional photonic crystals sustaining bloch surface waves. I. Theory *J. Phys. Chem. C* **123** 21167–75
[10] Pellegrini G, Finazzi M, Celebrano M, Duò L and Biagioni P 2017 Chiral surface waves for enhanced circular dichroism *Phys. Rev. B* **95** 1–5
[11] Mogni E *et al* 2022 One-dimensional photonic crystal for surface mode polarization control *Adv. Opt. Mater.* **10** 2200759
[12] Konopsky V N and Alieva E V 2018 Photonic crystal surface mode imaging biosensor based on wavelength interrogation of resonance peak *Sens. Actuators B* **276** 271–8
[13] Rizzo R *et al* 2018 Bloch surface wave label-free and fluorescence platform for the detection of VEGF biomarker in biological matrices *Sens. Actuators B* **255** 2143–50
[14] Frascella F *et al* 2015 Enhanced fluorescence detection of miRNA-16 on a photonic crystal *Analyst* **140** 5459–63
[15] Lereu A L, Zerrad M, Passian A and Amra C 2017 Surface plasmons and Bloch surface waves: towards optimized ultra-sensitive optical sensors *Appl. Phys. Lett.* **111** 011107
[16] Santi S *et al* 2013 Real-time amyloid aggregation monitoring with a photonic crystal-based approach *Chem. Phys. Chem.* **14** 3476–82
[17] Michelotti F, Rizzo R, Sinibaldi A, Munzert P, Wächter C and Danz N 2017 Design rules for combined label-free and fluorescence bloch surface wave biosensors *Opt. Lett.* **42** 2798–801
[18] Tang Y and Cohen A E 2010 Optical chirality and its interaction with matter *Phys. Rev. Lett.* **104** 1–4
[19] Tang Y and Cohen A E 2011 Enhanced enantioselectivity in excitation of chiral molecules by superchiral light *Science* **332** 333–6
[20] Boyd R W and Sipe J E 1994 Nonlinear optical susceptibilities of layered composite materials *J. Opt. Soc. Am. B* **11** 297
[21] Cheben P, Halir R, Schmid J H, Atwater H A and Smith D R 2018 Subwavelength integrated photonics *Nature* **560** 565–72
[22] Hao C, Zhang J, Yang B, Wang M, Zheng W and Liu A 2025 Active resonant modes in the metastructure composed of a surface subwavelength grating and a vertically layered structure *J. Phys. D: Appl. Phys.* **58** 135112
[23] Michelotti F, Sinibaldi A, Munzert P, Danz N and Descrovi E 2013 Probing losses of dielectric multilayers by means of Bloch surface waves *Opt. Lett.* **38** 616–8
[24] Moharam M G, Gaylord T K, Pommet D A and Grann E B 1995 Stable implementation of the rigorous coupled-wave analysis for surface-relief gratings: enhanced transmittance matrix approach *J. Opt. Soc. Am. A* **12** 1077
[25] Kong W, Zheng Z, Wan Y, Li S and Liu J 2014 High-sensitivity sensing based on intensity-interrogated Bloch surface wave sensors *Sens. Actuators B* **193** 467–71
[26] Autere A *et al* 2015 Slot waveguide ring resonators coated by an atomic layer deposited organic/inorganic nanolaminate *Opt. Express* **23** 26940